The Astronomical Journal, 148:51 (12pp), 2014 September doi:10.1088/0004-6256/148/3/51

A *uvbyCa*Hβ ANALYSIS OF THE OLD OPEN CLUSTER, NGC 6819*

Barbara J. Anthony-Twarog[1], Constantine P. Deliyannis[2], and Bruce A. Twarog[1]
[1] Department of Physics and Astronomy, University of Kansas, Lawrence, KS 66045-7582, USA; bjat@ku.edu, btwarog@ku.edu
[2] Department of Astronomy, Indiana University, Bloomington, IN 47405-7105, USA; cdeliyan@indiana.edu
Received 2014 April 29; accepted 2014 June 17; published 2014 August 7

ABSTRACT

NGC 6819 is a richly populated, older open cluster situated within the Kepler field. A CCD survey of the cluster on the *uvbyCa*Hβ system, coupled with proper-motion membership, has been used to isolate 382 highly probable, single-star unevolved main-sequence members over a 20′ field centered on the cluster. From 278 F dwarfs with high precision photometry in all indices, a mean reddening of $E(b-y) = 0.117 \pm 0.005$ or $E(B-V) = 0.160 \pm 0.007$ is derived, where the standard errors of the mean include both internal errors and the photometric zero-point uncertainty. With the reddening fixed, the metallicity derived from the same 278 stars is [Fe/H] $= -0.116 \pm 0.101$ from m_1 and -0.055 ± 0.033 from hk, for a weighted average of [Fe/H] $= -0.06 \pm 0.04$, where the quoted standard errors of the mean include the internal errors from the photometric scatter plus the uncertainty in the photometric zero points. If metallicity is derived using individual reddening values for each star to account for potential reddening variation across the face of the cluster, the analogous result is unchanged. The cluster members at the turnoff of the color–magnitude diagram are used to test and confirm the recently discovered variation in reddening across the face of the cluster, with a probable range in the variation of $\Delta E(B-V) = 0.045 \pm 0.015$. With the slightly higher reddening and lower [Fe/H] compared to commonly adopted values, isochrone fitting leads to an age of 2.3 ± 0.2 Gyr for an apparent modulus of $(m-M) = 12.40 \pm 0.12$.

Key words: open clusters and associations: general – open clusters and associations: individual (NGC 6819)

Online-only material: color figures, machine-readable and VO tables

1. INTRODUCTION

While the mantra of a common distance, age, and composition is invariably cited to justify the study of star clusters as testbeds of stellar evolution, the reality imposed by cluster dynamical evolution within a Galactic gravitational potential well often limits the application of these admittedly valuable characteristics. The typical timescale for evaporation of open clusters is only a few $\times 10^8$ yr, as confirmed by statistical studies of star clusters within a few hundred parsecs of the Sun (Lamers et al. 2005), while for clusters interior to the solar circle, the decline in numbers beyond 1 Gyr in age is even more dramatic (Janes & Phelps 1994; Carraro et al. 2014). For clusters at greater distance, contamination of sparsely populated regions of the color–magnitude diagram (CMD) by field stars, sometimes complicated by differential reddening, can make delineation of the more rapid phases of post-main-sequence evolution an exercise in self-delusion. These limitations heighten the impact of any richly populated, nearby open cluster older than 2 Gyr, as exemplified by the prolific literature on iconic clusters such as M67 and NGC 188 and, more recently, NGC 2420 and NGC 6791. A surprisingly understudied cluster for many years was NGC 6819 (Burkhead 1971; Auner 1974), surprising because of its extremely rich, well-defined CMD from the main sequence to the tip of the giant branch within the underpopulated cluster age range of 2–4 Gyr. Its profile has changed dramatically in the last few years due to its inclusion within the Kepler field, making it the focus of asteroseismic studies reaching down the giant branch (Stello et al. 2011), with a rapidly expanding literature related to the cluster and its members (Anthony-Twarog et al. 2013; Jeffries et al. 2013; Platais et al. 2013; Yang et al. 2013; Wu et al. 2014a, 2014b).

With the goal of using atmospheric Li to probe stellar structure and evolution among low-mass stars, the authors have undertaken an extensive spectroscopic program to survey members of a key set of open clusters from the tip of the giant branch to as far down the main sequence as the technology allows. First results have been published for the clusters NGC 3680 (age = 1.75 Gyr; Anthony-Twarog et al. 2009) and NGC 6253 (3.0 Gyr; Anthony-Twarog et al. 2010; Cummings et al. 2012). Among the clusters currently under analysis are NGC 7789 (1.5 Gyr) and NGC 6819 (2.3 Gyr), with over 300 stars observed in each. The age of NGC 6819 places the turnoff stars in a mass range where partial degeneracy at hydrogen exhaustion slows the evolutionary rate enough to populate both the subgiant branch and the first-ascent giant branch below the red giant clump. Preliminary spectroscopic analysis has already led to the discovery of a unique Li-rich giant fainter than the level of the clump (Anthony-Twarog et al. 2013), below the point where standard stellar evolution models predict the initiation of mixing assumed to create Li-rich atmospheres.

However, high dispersion spectroscopic analysis requires reliable input parameters for the models used in interpreting the spectra, specifically temperatures and surface gravities. These, in turn, demand precise estimates of the cluster reddening and distance, usually derived from comparison of the observed CMD to theoretical isochrones of appropriate age and metallicity. The goal of this paper is to define the fundamental properties of NGC 6819 through an analysis of the cluster on the *uvbyCa*Hβ photometric system. The efficacy of this approach has been demonstrated many times in the past, including studies of NGC 5822 (Carraro et al. 2011), NGC 6253 (Twarog et al. 2003), NGC 6791 (Anthony-Twarog et al. 2007), and Mel 71 (Twarog et al. 2006). Of particular value for open clusters in rich and extended fields is the photometric capability to derive individual reddening estimates while eliminating probable field

* WIYN Open Cluster study LXI.

stars which may have proper motions consistent with cluster membership, a point we will return to in Section 3.

The outline of the paper is as follows. Section 2 discusses the CCD observations and their reduction to the standard system for intermediate-band photometry; Section 3 uses the photometry, in conjunction with proper-motion membership, to identify and isolate probable cluster members which become the core data set for selecting single, main-sequence stars for reddening and metallicity estimates in Section 4. We also test (and confirm) the existence of the reddening gradient across the face of the cluster as derived by Platais et al. (2013, hereinafter referred to as PL). Section 5 contains a discussion of the potential impact of the new reddening and metallicity on the cluster distance and age and a summary of our conclusions.

2. OBSERVATIONS AND DATA REDUCTION

2.1. Observations

Intermediate and narrowband imaging of NGC 6819 was completed using the WIYN 0.9 m telescope on UT dates 2011 July 2–7, 2012 June 14–20, and 2013 June 8–13. Fourteen of these 19 nights were usable for photometry but only a few were totally photometric. For all nights other than five during the 2012 June run, the S2KB CCD was used at the $f/7.5$ focus of the telescope for a $20' \times 20'$ field with $0.6''$ pixels. $vbyCa\mathrm{H}\beta$ data from five of the nights in 2012 were obtained using the smaller T1KA chip with identical pixel size. The point-spread function (PSF)-based photometry for each smaller frame for each filter was transformed to the instrumental system of the S2KB chip using a linear calibration and a color term coupled to $(b - y)$. However, the standard stars observed during these five nights have not been utilized for calibration purposes; only standards observed with the S2KB chip have been used for calibration. All seven filters are from the $3'' \times 3''$ filter set owned jointly by the University of Kansas and Mt. Laguna Observatory.

Bias frames and dome flats for each filter were obtained every night, with sky flats observed at twilight for the u, v, and Ca filters when feasible. On all photometric nights, fields in NGC 6819, as well as standard stars and extinction stars, were observed over a range in air mass. Extinction coefficients were separately determined for each photometric night.

Standard IRAF routines were used to perform initial processing of the frames, i.e., bias subtraction and flat fielding. Illumination corrections were applied for frames obtained in 2013 and for the shortest wavelength frames obtained in 2012. A fairly comprehensive discussion of our procedure for obtaining PSF-based instrumental magnitudes and merging multiple frames of a given filter can be found in Anthony-Twarog & Twarog (2000).

Our calibrations to the standard extended Strömgren system are based on aperture photometry in the program cluster, of field star standards, and of stars in NGC 6633 for each photometric night. For every frame contributing to the photometric calibration solution, aperture magnitudes for standard stars are obtained within apertures scaled to five times the FWHM for the frame; sky annuli are uniformly chosen with the inner radius one pixel larger than the aperture and a uniform annular width. A number of sources were consulted for field star standard index values, including the catalog of Twarog & Anthony-Twarog (1995) for V, $b - y$ and hk indices, catalogs of $uvby\mathrm{H}\beta$ observations by Olsen (1983, 1993, 1994), and compilations of Hβ indices by Hauck & Mermilliod (1998) and Schuster & Nissen (1989). Hβ indices for stars in NGC 6633, obtained by Schmidt (1976), were used to augment the field star standards in calibrating Hβ indices.

Table 1
Characterization of Calibration Equations

Index	Class	N_{nights}	$N_{\mathrm{pe\ Stds}}$	α	γ	σ_1	σ_2	sem
V	···	4	6–15	1.0	0.045	0.027	0.024	0.005
$b - y$	BD/RG	4	4–12	0.993	···	0.016	0.007	0.003
$b - y$	RD	4	2–4	0.860	···	0.048	0.006	0.004
m_1	BD	3	2–4	1.0	···	0.053	0.028	0.008
m_1	RG	3	2–6	1.0	−0.09	0.029	0.031	0.010
m_1	RD	3	2–5	1.0	···	0.026	0.029	0.009
c_1	BD	3	2–4	1.0	···	0.031	0.017	0.035
c_1	RG	3	2–6	0.95	0.25	0.144	0.042	0.050
c_1	RD	3	2–4	1.0	···	0.183	0.040	0.031
hk	···	2	7–13	1.057	···	0.032	0.035	0.009
Hβ	···	1	33	1.125	···	0.017	···	0.003

Notes. Calibration equations for index x are of the form $x_{\mathrm{std}} = \alpha\ x_{\mathrm{instr}} + \gamma(b - y)_{\mathrm{instr}} + \beta$. Classes of stars include warm dwarfs BD, cool dwarfs RD, and cool giants RG. σ_1 describes greatest dispersion of standard star values with respect to the calibration equation for any night incorporated in the calibration; σ_2 indicates the dispersion among individual nights' calibration equation zero points; the sem column denotes the standard error of the mean calibration equation zero-point value.

Following standard procedures for Strömgren photometry, a single $b - y$ calibration equation was derived for warmer dwarfs and giant stars and a separate calibration equation for dwarfs with $(b - y)_0 \geqslant 0.42$. Calibrations of m_1 and c_1 for cooler giants are determined independently from calibrations applied to bluer dwarfs or calibrations applied to cooler main sequence stars. All photoelectric standards, field stars and cluster stars alike, were used to determine slopes and color terms for the calibration equations, summarized in Table 1. An independent zero point was determined for each calibration equation on each night, based on field star standards, with the exception that stars in NGC 6633 were used as Hβ standards for the one photometric night contributing to the calibration of Hβ indices.

As is our usual procedure, we extend the calibration equations to the indices for NGC 6819 stars based on merged profile-fit photometry by determining the average differences between profile-fit indices and indices determined from aperture photometry in the cluster on each photometric night. These data presented an unusually challenging case for this aperture correction scheme, caused jointly by moderately poor seeing on some nights and a relatively crowded cluster core field. It was necessary to determine the average difference between the aperture and profile-fit indices based on carefully selected—and not very large—sets of stars for which no neighbors would be included inside apertures of $\sim 20''$ radius. With such aperture corrections, the calibration equations from each photometric night may be applied to the aperture photometry in the program cluster, and then by extension to the profile-fit indices in NGC 6819, with an independent zero point determined for each equation from each photometric night.

Several indicators of the precision of the calibration equations' zero points are presented in Table 1. For each photometric night, σ_1 quantifies the dispersion of calibrated values about standard values for field star standards; σ_2 quantifies the dispersion among zero points for the several photometric nights. Both σ values are standard deviations. The final calibration equation's zero point is determined from a weighted sum of the independent night evaluations; the final statistic labeled "sem" denotes the standard error of the weighted mean.

Table 2
*uvbyCa*Hβ Photometry of Stars in the Field of NGC 6819

α(2000)	δ(2000)	Prob.	V	$b-y$	m_1	c_1	hk	Hβ	σ_V	σ_{by}	σ_{m1}	σ_{c1}	σ_{hk}	σ_β	N_y	N_b	N_v	N_u	N_{Ca}	N_n	N_w
295.18539	40.30586	···	9.532	0.088	0.156	1.077	0.309	2.843	0.004	0.010	0.014	0.012	0.014	0.014	4	6	8	6	5	10	7
295.11700	40.34310	···	9.610	0.985	0.728	−0.317	···	2.518	0.001	0.002	0.006	0.009	0.018	0.015	4	4	2	2	1	9	8
295.48468	40.31559	3	9.660	0.371	0.177	0.397	0.646	2.580	0.002	0.004	0.008	0.010	0.006	0.009	4	4	7	7	10	10	7
295.17383	40.28929	···	9.773	0.284	0.111	0.586	0.385	2.651	0.001	0.004	0.007	0.006	0.006	0.012	5	7	8	7	8	10	8
295.39954	40.16243	···	10.522	1.444	−1.296	1.927	−0.245	2.861	0.046	0.060	0.077	0.060	0.076	0.054	4	12	16	12	22	12	14
295.17725	40.05150	0	10.830	0.633	0.371	0.505	1.109	2.521	0.002	0.003	0.005	0.005	0.005	0.005	10	11	13	14	20	16	16
295.51831	40.24933	99	10.830	1.286	−0.185	0.759	0.956	2.734	0.042	0.053	0.066	0.052	0.064	0.055	9	16	13	14	20	17	16
295.35254	40.05614	0	10.967	0.683	0.332	0.509	1.116	2.527	0.003	0.003	0.005	0.005	0.004	0.003	13	13	13	14	20	17	15
295.25128	40.23014	0	10.987	0.366	0.150	0.465	0.584	2.636	0.004	0.007	0.011	0.010	0.011	0.008	18	16	21	14	29	24	23
295.28415	40.32453	···	11.181	1.063	0.690	−0.293	1.790	2.611	0.006	0.008	0.010	0.010	0.009	0.009	14	17	13	14	20	17	16
295.47934	40.23945	99	11.187	1.099	0.624	−0.271	1.718	2.625	0.005	0.007	0.011	0.015	0.011	0.009	15	17	13	14	20	17	16
295.32315	40.17828	0	11.361	1.202	0.106	···	1.193	2.719	0.005	0.008	0.023	0.049	0.023	0.007	23	15	4	1	4	25	24
295.42532	40.30449	5	11.418	0.523	0.211	0.524	0.664	2.610	0.001	0.002	0.004	0.005	0.003	0.004	15	16	13	14	20	17	16
295.39221	40.05499	0	11.473	0.321	0.124	0.485	0.439	2.651	0.002	0.003	0.005	0.005	0.004	0.005	17	15	13	14	20	17	16
295.29922	40.22464	99	11.528	1.119	0.524	0.257	1.801	2.605	0.002	0.003	0.006	0.010	0.005	0.005	25	25	22	14	29	25	24
295.29578	40.18643	99	11.629	0.715	0.361	0.526	1.126	2.571	0.003	0.003	0.006	0.007	0.005	0.005	24	25	22	14	30	25	24
295.29630	40.19488	99	11.636	0.809	0.495	0.417	1.327	2.559	0.002	0.003	0.005	0.006	0.004	0.004	24	22	22	14	30	25	20
295.39288	40.29617	99	11.647	0.978	0.698	0.172	1.790	2.536	0.002	0.003	0.005	0.006	0.005	0.005	17	17	13	14	21	19	17
295.32086	40.18101	99	11.680	1.020	0.652	0.140	1.764	2.572	0.002	0.003	0.005	0.008	0.006	0.004	25	25	22	13	26	25	24
295.21530	40.11550	99	11.681	0.423	0.182	0.398	0.697	2.602	0.004	0.006	0.010	0.009	0.008	0.005	24	20	22	14	30	25	24

(This table is available in its entirety in machine-readable and Virtual Observatory (VO) forms in the online journal. A portion is shown here for guidance regarding its form and content.)

Final photometry on the *uvbyCa*Hβ system can be found in Table 2, where most columns are self-explanatory: (X, Y) CCD positions have been translated to the right ascension and declination coordinate frame of PL. As described further in Section 3, we were able to match a majority of our photometric sample to the positions and photometry presented in PL; membership probabilities for the nearly 4000 matched stars are included in Table 2 where available. Stars are included in Table 2 only if they were observed at least twice in both y and b filters to construct V and $b-y$, twice each in v, Ca, and u for m_1, hk, and c_1, respectively. Two observations each in the narrow and wide filter were required for the Hβ index to be retained. Standard errors of the mean for the indices are calculated by combining the errors for individual filters in quadrature and are defined solely by the internal, i.e., frame-to-frame, precision of the of the individual filters. The increase in scatter among the indices for the brightest stars is due the inclusion of two bright, very red giants that exhibit apparent variability and to the reduced number of CCD frames with exposure times short enough to leave the brightest stars unsaturated. A plot of the average *sem* for each index as a function of V can be seen in Figure 1. The longer, online version of Table 2 includes photometry for 7187 stars, subject to the limitations described above as well as restriction to stars with $\sigma_{b-y} \leqslant 0.10$.

2.2. Comparison to Previous Photometry

Our V magnitudes can be compared directly to the three comprehensive broadband surveys to date which include V photometry (Rosvick & VandenBerg 1998; Kalirai et al. 2001; Yang et al. 2013, hereinafter referred to as RV, KA, and YA, respectively) with some surprising results. Beginning with RV, in the bottom panel of Figure 2 we show the residuals in V, in the sense (RV − Table 2), for 1690 stars matched via the WEBDA (X, Y) coordinates for RV and our data. No known variables or stars with larger than average errors have been eliminated from the figure. The overall pattern exhibits a mean offset close to 0.00 at all magnitudes with increasing scatter as V approaches 18. Somewhat surprising is the dispersion in the residuals among the brighter stars. One would expect that, given the high precision of both photometric surveys at $V = 16$ and brighter, the trend should narrow significantly toward smaller V.

After running a number of tests, the source of the scatter emerged as a gradient in the V photometry with right ascension or X in WEBDA coordinates. Using 566 stars brighter than $V = 16$ to minimize the impact of larger photometric scatter, we plot the residuals in V as a function of X CCD position in the top panel of Figure 2. The trend is obvious and is confirmed even if stars at all magnitudes are included. Fitting a linear relation to the data, the residual gradient becomes

$$\Delta V = (0.003 \pm 0.001) - (0.043 \pm 0.002) \times X(\text{kilopixels})$$

Applying this to the photometry of RV, the revised residual plot is shown in the middle panel of Figure 2. The improvement is obvious; the mean residual is, by definition, 0.000 with a dispersion of only ±0.016 for $V \leqslant 16$ and ±0.029 for all stars in the sample. Again, using only stars brighter than $V = 16$, no correlations of significance were found for the residuals with either $B - V$ color or declination (Y). We can attribute the trend to the photometry of RV because a comparison between KA and RV shows the same gradient. We also note that position-dependent gradients of similar size have been identified in the broadband data of Gim et al. (1998) for NGC 7789 (Brunker et al. 2013).

Turning next to KA, we plot in Figure 3 the residuals in V, in the sense (KA; Table 2), for 1819 stars common to the two surveys. We emphasize that the residuals have a slightly larger range than in Figure 2 and no stars with residuals more negative than −0.10 mag have been excluded from the plot. Two trends are obvious.

1. There is a distinct dichotomy among the stars above and below $V = 14$. The mean offset among the brighter sample

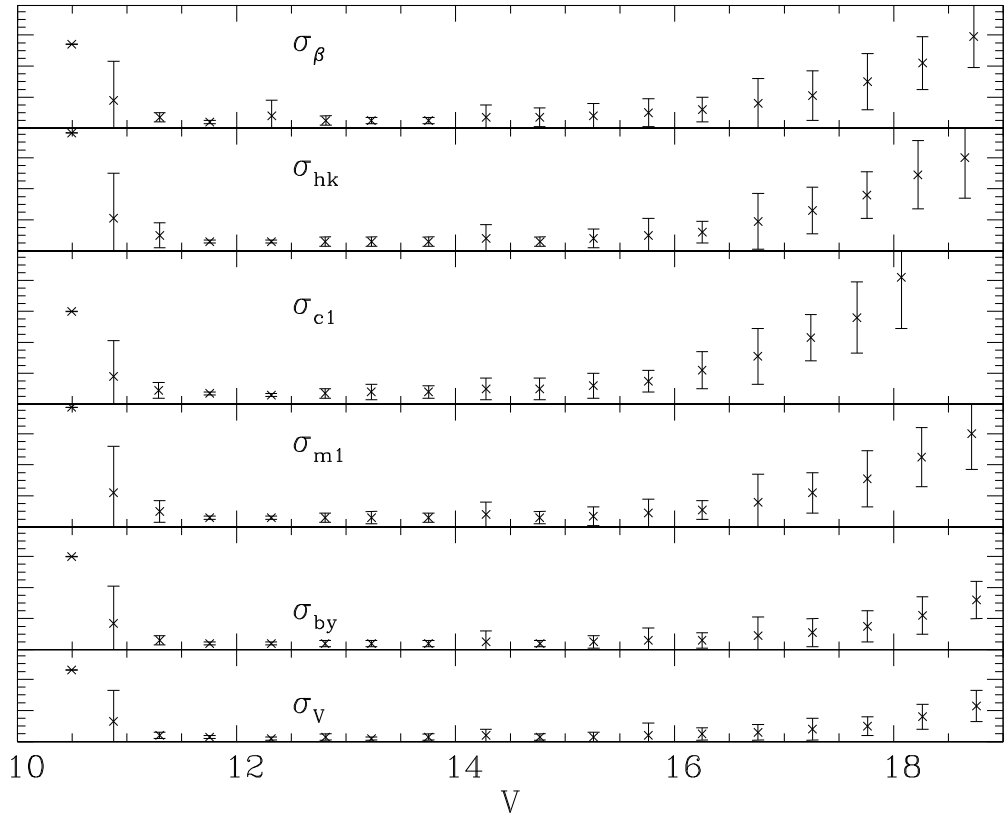

Figure 1. Average photometric errors in V, $(b-y)$, m_1, c_1, hk, and $H\beta$ as a function of the V magnitude. The panel heights are scaled proportionately to the physical range, with major tick marks indicative of 0.02 mag.

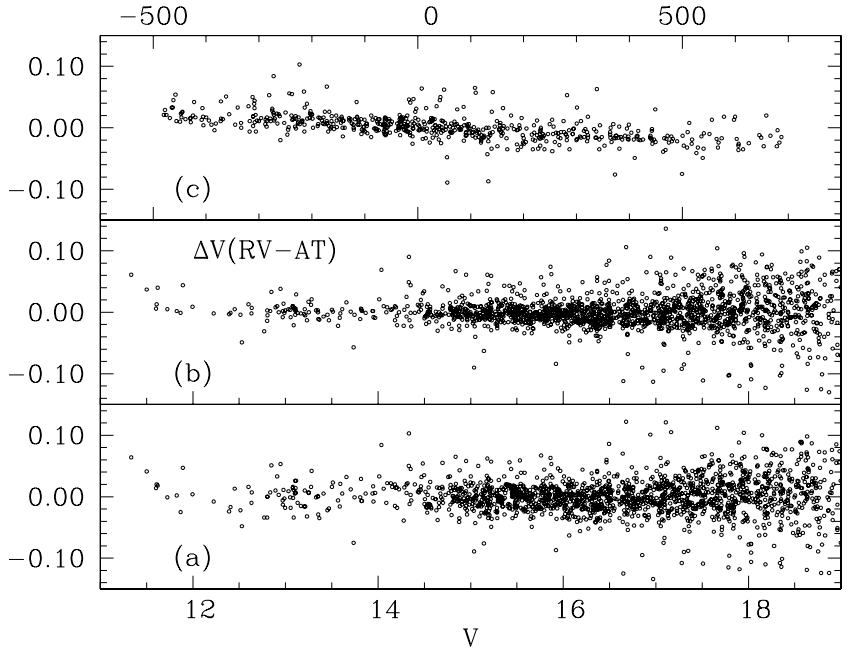

Figure 2. (a) Residuals in ΔV as a function of V for (RV; Table 1); (b) same as (a) after correction for the trend in (c), which shows residuals in ΔV as a function of WEBDA coordinate X.

is about −0.01 mag but the scatter is excessive, while the fainter sample shows a mean offset closer to 0.02 mag.

2. Among the fainter stars, the dispersion is highly asymmetric, with a long and well-populated tail toward larger residuals, virtually independent of the magnitude.

Both of these trends are confirmed through comparisons between RV and KA, with or without a spatial correction to the data of RV. Among the brighter sample, there is weak evidence for a spatial dichotomy in the photometric zero point coupled to declination, with stars in the north being offset from those in the southern half of the field by 0.03 to 0.04 mag, but the sample is small. For the stars fainter than $V = 14$, no obvious spatial gradient emerges which would explain the extended tail toward positive residuals. The asymmetry may be a reflection of the way in which crowded stellar images have been handled

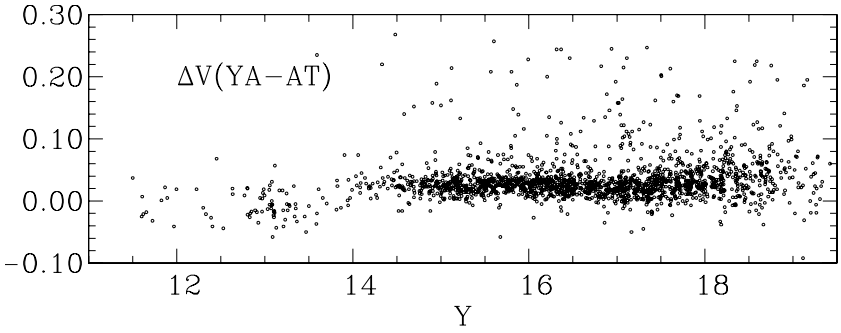

Figure 3. Residuals in ΔV as a function of V in the sense (KA; Table 1). The physical scale matches that of Figure 2.

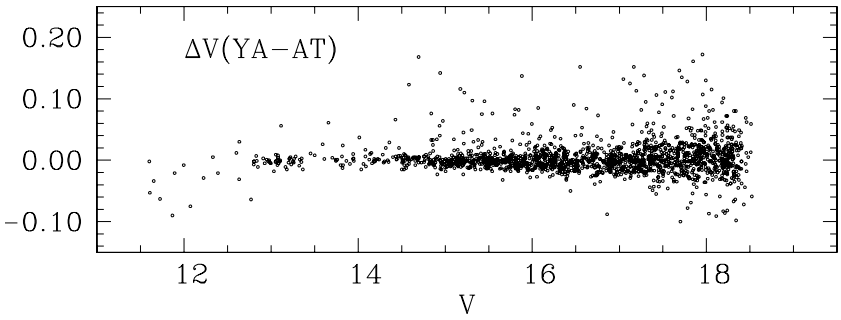

Figure 4. Residuals in ΔV as a function of V in the sense (YA; Table 1). The physical scale matches Figures 2 and 3.

by the PSF software. KA provided no comparisons with the photometry of RV so this issue was never addressed.

The third and final large survey is that of YA in *VI*. While YA include some discussion of the residuals between their work and earlier studies, noting good agreement, their comparison sample includes fewer than 100 stars, more than an order of magnitude fewer than we can readily find in common with RV and KA. The reason for this deficiency remains a mystery. For comparison purposes, the data of Table 2 were cross-matched with those of KA after the CCD coordinates for both samples were transformed to right ascension and declination, as defined in PL. Using a match radius of $1''$ and eliminating any stars with magnitude differences greater than 0.2 mag to minimize mismatches leaves a common sample of 1619 stars to $V = 18.5$. The residuals in V, in the sense (YA; Table 2), are plotted in Figure 4. The agreement with YA is excellent, with a modest asymmetry to the positive side of the residuals. From 516 stars brighter than $V = 16.0$, the mean offset is $+0.003 \pm 0.023$; for all 1619 stars, the mean residual is $+0.004 \pm 0.028$, where the quoted errors are standard deviations.

We conclude that our V photometry is on the same system as YA and RV, corrected for a spatial gradient, to better than a few millimagnitudes in the mean. By contrast, the sample of KA exhibits a distinct change in zero point at $V \sim 14$, with the fainter sample approximately 0.03 mag too faint relative to the other three studies.

3. THE COLOR–MAGNITUDE DIAGRAM

The CMD based upon $(V, b - y)$ for all stars in Table 2 is shown in Figure 5. Stars with *sem* errors in $b - y$ below 0.015 are shown as open circles, while stars with errors greater than this cutoff to an *sem* limit of 0.15 mag are plotted as crosses. While some primary features of the CMD, the location of the turnoff and the red giant clump, are obvious, due to the area of the sky covered by the frames, field star confusion makes delineation of the giant branch below the clump and the fainter main sequence almost impossible.

As a first attempt to minimize the field star contamination, we plot in Figure 6 all stars within $5'$ of the cluster center as defined by PL. The improvement in isolating the cluster is readily apparent, though the reduction in both field stars and cluster members for $V \geqslant 18$ still leaves a respectable level of contamination. The cluster core exhibits a rich population of blue stragglers, a well-defined red clump and bright giant branch, but a non-negligible degree of confusion among potential subgiants and first-ascent red giants below the clump.

Fortunately, the astrometric analysis of the cluster by PL supplies proper-motion membership for the majority of the stars in our field. As stated in Section 2, we have transformed our CCD (X, Y) coordinates to the (R.A., decl.) system of PL, which should be J2000, epoch 2009.875. As a first step, all stars' coordinates common to both data sets and coincident within a radial distance of $2''$ were identified. Next, the stars common to YA and PL were used to derive a transformation between the g, $g - r$ photometry of PL and the V, $V - I$ data of YA. From 1250 stars brighter than $V = 18$, we found

$$V = g - (0.038 \pm 0.006) - (0.595 \pm 0.018)(g - r) + (0.061 \pm 0.012)(g - r)^2,$$

$$V - I = (0.403 \pm 0.010) - (0.408 \pm 0.029)(g - r) + (0.358 \pm 0.020)(g - r)^2.$$

The dispersions among the residuals in ΔV and $\Delta(V - I)$ are 0.022 mag and 0.029 mag, respectively. With the transformed g photometry in hand, any star common to PL and Table 2 through R.A. and decl. which showed a difference in V greater than 0.1 mag was excluded from the sample. Finally, all stars with membership probabilities less than 50% were excluded. Three stars brighter than $V = 17$ with proper-motion probabilities above 50% which had been excluded due to an excessive V

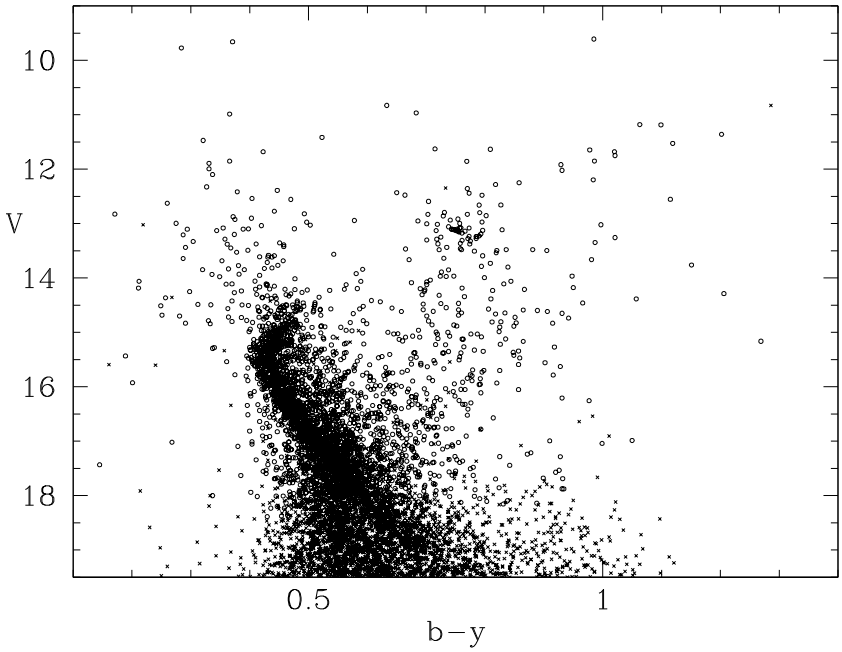

Figure 5. CMD for all stars in Table 1. Open circles are stars with photometric errors in $b - y \leqslant 0.015$. Crosses are stars with errors in $b - y$ larger than 0.015.

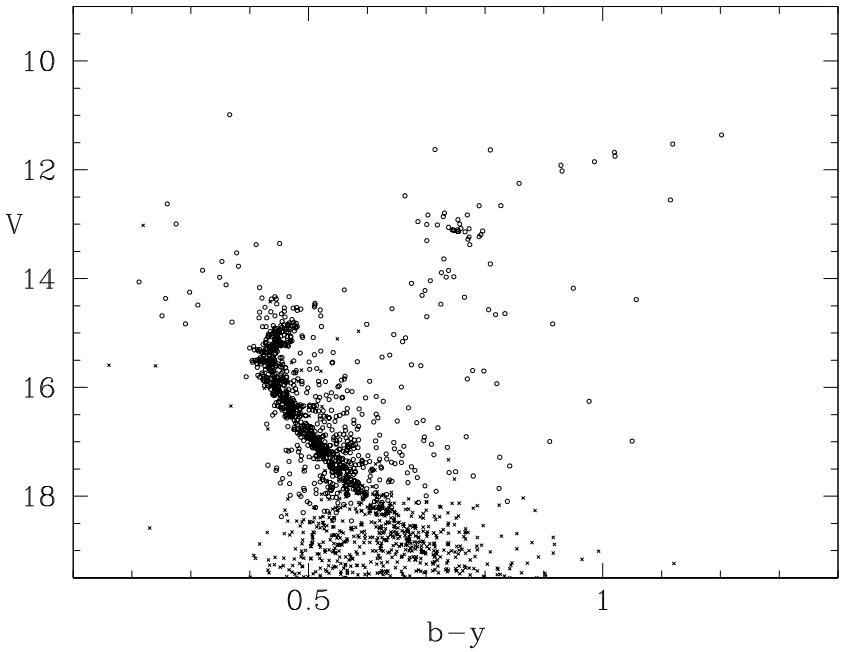

Figure 6. Same as Figure 5, but for all stars within 5′ of the cluster core.

residual were reinstated. All other excluded stars from the original match are either fainter than $V = 17$ and/or have membership probabilities below 50%. The resulting (V, $b - y$) CMD for all members within the CCD frames is given in Figure 7. Symbols have the same meaning as before, but the sample has been cut at $V = 19$ to reduce scatter caused by increasing errors in $b - y$.

The improvement relative to even Figure 6 is dramatic. While all the primary features from the core sample CMD remain, a plausible outline of the subgiant branch and first-ascent giant branch below the clump now emerges. The main sequence is tightly defined, with only a modest level of scatter to the red, as expected for the band defined by probable binaries extending up to 0.75 mag above the unevolved main sequence. The unevolved main sequence can now be traced down to the limit of the plot, though it is apparent that some of the background field stars with proper motions comparable to the cluster still remain near $b - y = 0.5$, as well as their evolved counterparts in the vertical band between $b - y = 0.7$ and 0.8.

4. CLUSTER PROPERTIES—REDDENING AND METALLICITY

With the restricted sample of Figure 7, we can now approach the photometric reddening and metallicity estimate. Reddening on the $uvbyH\beta$ system is defined by comparison of the predicted $b - y$ color tied to the stellar temperature as derived from the reddening-free Hβ index, adjusted for evolutionary effects and

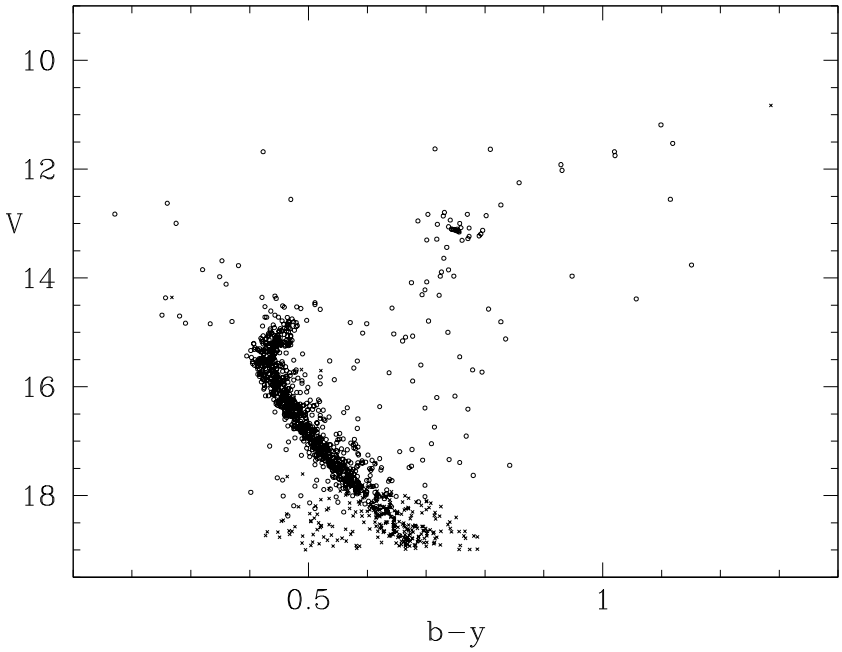

Figure 7. Same as Figure 5, but for all stars with proper-motion membership above 50%.

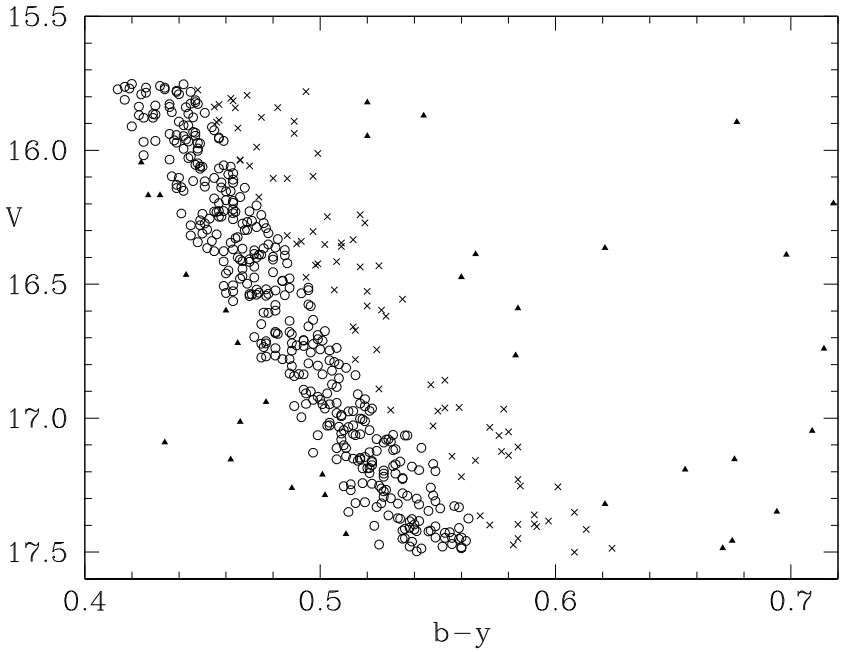

Figure 8. Unevolved $(V, b-y)$ main sequence of Figure 7. Open circles are probable single stars or binaries with small mass ratios, crosses are potential binaries with q closer to 1.0, and filled triangles are likely non-members.

metallicity, to the observed $b-y$ index for each F and early G cluster dwarf. Potential sources of scatter in the final cluster averages include poor photometry, non-members, composite systems with distorted photometry, and inadequate correction for the effects of post-main-sequence evolution. As we have done consistently in the past, our approach is to eliminate any stars which, for any of the reasons noted above, might reduce the reliability or skew the estimate of the final cluster parameters. The first simple cut is to eliminate all stars brighter than $V = 15.75$, i.e., stars significantly evolved beyond the main sequence and/or populating the turnoff in a region likely to be contaminated by the extended binary sequence, and all stars fainter than $V = 17.50$, where photometric errors in indices other than $b-y$ begin to grow rapidly with increasing magnitude. An expanded $(V, b-y)$ CMD for this sample is shown in Figure 8.

The delineation of a tight main sequence with a full range of only 0.03 to 0.04 mag in $b-y$ at a given V is encouraging, though some stars do lie well off the main sequence. To isolate likely single *member* stars, we have drawn a mean linear relation through the main sequence and tagged any star within 0.02 mag at each V as a probable single-star member (open circles). Stars 0.02 to 0.07 mag redder than the mean relation are defined as probable binaries (crosses); stars at least 0.02 bluer than or $\geqslant$0.07 mag redder than the main line are tagged as probable non-members (filled triangles). This leads to a sample of 382 probable single-star (or binaries with low mass ratios) members.

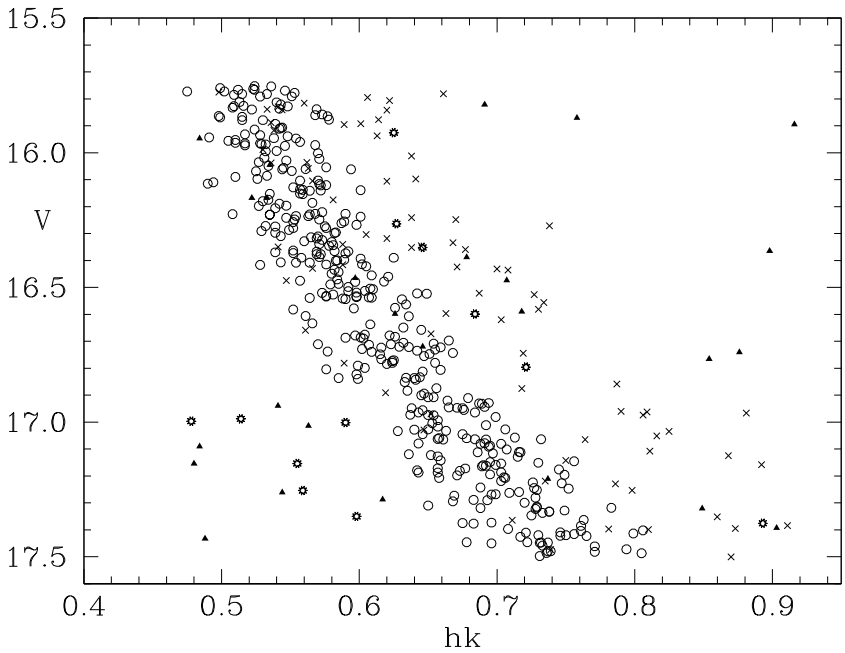

Figure 9. Unevolved (V, hk) main sequence for stars of Figure 7. Symbols have the same meaning as for Figure 8, with the open starburst symbols denoting additional deviants for removal.

An immediate question in light of claims for potential reddening variation across the face of the cluster (PL) is whether or not the red limit eliminates true cluster members with higher than average reddening rather than binaries or non-members. Fortunately, hk photometry offers an effective resolution. The hk index is designed to supply a metallicity estimate for stars of a given temperature but, for stars of a given metallicity, it is a strong function of temperature. However, unlike $b-y$, hk is only weakly dependent on reddening, with $E(hk) = -0.16E(b-y)$. Thus a star which appears too red at a given V in Figure 8 because it is intrinsically cooler will shift in a (V, hk) diagram by an even larger amount. If the star is shifted in $b-y$ due to enhanced reddening, the shift in (V, hk) will be small to negligible and toward the blue, i.e., smaller hk. The (V, hk) diagram is shown in Figure 9; symbols have the same meaning as in Figure 8. All stars with errors in hk larger than 0.03 mag have been eliminated, reducing the sample by 17 stars, including four stars classed as singles in Figure 9. While some stars classed as deviants in Figure 8 do lie on the main sequence in Figure 9, the classifications for the majority are confirmed. Additionally, a half dozen stars below $V = 16.9$ appear significantly bluer than expected (filled circles). Based upon Hβ and m_1 indices, these are either metal-deficient background stars or heavily reddened, hotter dwarfs; neither group contains probable cluster members. Based upon the positions in Figure 9, we eliminate 12 additional stars which may be binaries or field stars, leaving a sample of 366 stars.

To ensure that only the most precise photometry is included in the analysis, we eliminate all stars with errors in Hβ, m_1, and hk larger than 0.02 mag, 0.02 mag, and 0.03 mag, respectively. Finally, color transformations between Hβ and $b-y$ invariably include a correction for evolution, defined via the c_1 index, with more evolved stars having larger c_1 values than an unevolved star on the main sequence. While the majority of stars in our restricted sample have measured c_1 indices, since we are extending the data below $V = 16.5$, the errors in c_1 grow rapidly with increasing V, as indicated by Figure 1. To avoid elimination of a large fraction of the data set, we have chosen to adopt the c_1 value at the observed Hβ as defined by the standard relation as the reddening-corrected c_1 index for each star. In short, we have assumed that all stars are unevolved, in keeping with the restriction imposed by eliminating all stars brighter than $V = 15.75$.

As in past cluster analyses, use is made of two intrinsic Hβ-$(b-y)_0$ relations to define the intrinsic colors. The intrinsic $b-y$ color is derived in iterative fashion, starting with an assumed $E(b-y)$ and metallicity, calculating the cluster metallicity, redefining the intrinsic color for the calculated metallicity to obtain a new reddening, and repeating the sequence until the change in reddening is too small to be statistically significant. The first $E(b-y)$ from Olsen (1988) applies to F stars in the Hβ range from 2.58 to 2.72. From 278 F dwarfs that meet all the criteria, the mean $E(b-y)$ is found to be 0.115 ± 0.016 (sd). The second intrinsic color relation is that of Nissen (1988), a slightly modified version of the original relations derived by Crawford (1975, 1979) for F and A stars. For the same 278 F dwarfs, the alternate relation implies $E(b-y) = 0.119 \pm 0.017$ (sd). It should be noted that the slightly higher reddening for F stars using the Nissen (1988) relation compared to that of Olsen (1988) is a consistent occurrence from such comparisons (Twarog et al. 2006; Anthony-Twarog et al. 2007). A weighted average of the results leads to $E(b-y) = 0.117 \pm 0.002$ (sem), or $E(B-V) = 0.160 \pm 0.003$ (sem). When combined with the zero-point uncertainties in $b-y$ and Hβ, the total uncertainties in $E(b-y)$ and $E(B-V)$ become ± 0.005 mag and ± 0.007 mag, respectively. It should be emphasized that the dominant source of uncertainty in the reddening is the zero point of the $b-y$ photometry since the $(b-y)$, Hβ relation has a relatively shallow slope over the color range of interest, as seen in Figure 11 of Carraro et al. (2011).

With the reddening fixed, the next step is the derivation of metallicity, a parameter that can be defined using hk or m_1 coupled to either $b-y$ or Hβ as the primary temperature indicator. In past studies using $uvbyCa$Hβ photometry, the

metallicity from hk tied to Hβ invariably has been given the greatest weight due to the greater sensitivity of hk to modest metallicity changes, while the Hβ-based relations allow decoupling between errors in the two indices and minimize the impact of potential reddening variations, if any exist. We will follow the same approach with NGC 6819, allowing us to tie our results directly into the same metallicity scale from past intermediate-band cluster studies.

With $E(b-y) = 0.117$, the mean $\delta m_1(\beta)$ for 282 F dwarf probable members between H$\beta = 2.58$ and 2.72 is 0.025 ± 0.001 (sem), where $\delta m_1 = 0.0$ is set at the adopted Hyades metallicity of +0.12. On this same scale, NGC 3680, NGC 5822 and IC 4651 respectively have $\delta m_1 = 0.027 \pm 0.002$ (sem; Anthony-Twarog & Twarog 2004), $+0.017 \pm 0.003$ (sem) (Carraro et al. 2011), and 0.000 ± 0.002 (sem; Anthony-Twarog & Twarog 2000), implying that NGC 6819 is clearly lower in [Fe/H] than the Hyades, and almost as deficient as NGC 3680, a somewhat surprising result given the consistent claim that the cluster is metal-rich, a point we will return to in Section 4.2. The δm_1 measure translates to [Fe/H] $= -0.116 \pm 0.012$ (sem) on a scale where NGC 3680, NGC 5822, and IC 4651 have [Fe/H] $= -0.17$, -0.06, and +0.12, respectively. The translation from index to metallicity is partially dependent upon the mean color/temperature of the sample, which explains the modest shift in the relative ranking of the clusters in switching from index to [Fe/H]. As an additional reference point, the photoelectric $uvby$Hβ data of M67 produce [Fe/H] $= -0.06 \pm 0.07$ (Nissen et al. 1987). Taking into account the uncertainty in the zero point of the m_1 indices, [Fe/H] $= -0.12 \pm 0.10$ with internal and external errors combined.

Turning to the hk index for 282 stars, $\delta hk(\beta) = 0.050 \pm 0.003$ (sem), which translates to [Fe/H] $= -0.055 \pm 0.010$ (sem), on a scale where [Fe/H] = +0.12, 0.01, and -0.10 for the Hyades, NGC 5822, and NGC 3680. Taking errors in the hk zero points into account, [Fe/H] $= -0.06 \pm 0.03$, internal and external uncertainty combined. A weighted average of the two metallicity estimates leads to [Fe/H] $= -0.06 \pm 0.04$, where the errors refer to the combined internal and external errors from the combined indices.

Before discussing the significance of these results, an obvious question is the impact of variable reddening on our conclusions. For the [Fe/H] derived from hk, the impact is negligible. By definition, Hβ is reddening independent. If we include a range of 0.08 in $E(V-I)$ among the stars in the cluster, this translates to a range of 0.007 in $E(hk)$, or a spread of $\sim$0.025 in [Fe/H]. For m_1, the greater impact of reddening on the index coupled to a steeper δm_1–[Fe/H] relation translates the same reddening range to an [Fe/H] range seven times larger. Fortunately, we can derive the reddening for each star individually, rather than adopting the cluster mean for all stars, and recalculate the cluster metallicity. If we adopt the photometric reddening estimate from $b-y$, Hβ for each star, the resulting mean [Fe/H] from m_1 becomes -0.120 ± 0.013 while the analogous estimate from hk is [Fe/H] $= -0.055 \pm 0.011$ (sem), leading to a weighted average [Fe/H] $= -0.06 \pm 0.04$. Given the very modest range derived below for $E(b-y)$ and the impact of even small photometric scatter, the lack of a statistically significant change in the mean abundances is expected.

4.1. Reddening Variability

As discussed in Section 1, one of the potential sources of parametric scatter for a cluster spread over a field 20′ across at a distance of more than a kiloparsec is variable reddening along the line of sight. Due to the well-defined nature of the CMD at the turnoff plotted in Figure 7, we can immediately use the full width of the turnoff in $b-y$ at a fixed V to place an upper limit of 0.045 mag on the range in $E(b-y)$, 0.060 for $E(B-V)$, without applying any adjustment for photometric scatter in $b-y$ and/or contamination by a binary sequence. PL have used the VI data of YA for proper-motion members to define a blue edge in the (V, VI) CMD at the cluster turnoff, the color region where differential reddening effects should be maximized due to the combined shift in V and $V-I$. The color offset for each star relative to this fiducial relation is adopted as an estimate of the differential reddening, up to a limit of $\delta E(V-I) = 0.09$, where binaries may begin to dominate. The positional averages of these values are then used to construct a spatial reddening map (see Figure 10 of PL), showing that stars $\geqslant 2'$ east of the cluster center are typically 0.05 to 0.07 mag redder in $E(B-V)$ than the low reddening region in the southwest quadrant of the cluster, i.e., for stars $\geqslant 2'$ west and $\geqslant 2'$ south of the cluster center.

To test this claim, we have used the photometry defining Figure 7 and isolated two distinct samples. The group expected to be more highly reddened is composed of all stars $\geqslant 2'$ east of the cluster center while the predicted blue group encompasses stars in the southwest quadrant, $\geqslant 2'$ west and south of the cluster center. The CMD for the expanded region near the turnoff is shown in Figure 10(a) with the colors and symbol types indicating which reddening group the star belongs to (blue triangles or red crosses). The pattern is obvious; there is little doubt that the reddening trend established by PL is real. We can place a tight constraint on the size of the range between these two regions by shifting the blue stars appropriately in $b-y$ and V until the CMDs overlap. Figure 10(b) shows the impact of adding 0.022 (0.030) mag of reddening in $E(b-y)$ ($E(B-V)$) to the blue stars of the southwest quadrant. The scatter in the turnoff is cut in half, reduced almost to what one would expect from photometric scatter alone. Since the mean shift in color between the two regions should be less than the most extreme variation across the cluster, we estimate that the true spread in $E(B-V)$ lies somewhere between the 0.03 estimate above and the point-to-point range of 0.06 found by PL or $\Delta E(B-V) = 0.045 \pm 0.015$.

4.2. Previous Reddening and Metallicity Estimates

With the confirmation that NGC 6819 suffers from variable reddening in a range of 0.03 to 0.06 mag in $E(B-V)$, the import of past reddening estimates is reduced since the values derived will depend in part on where in the cluster the reddening was measured. A partial summary of derived and adopted reddening estimates for NGC 6819 can be found in Wu et al. (2014b). With the exception of two early studies by Auner (1974) and Lindoff (1972), and those studies which later adopted these flawed estimates (Friel & Janes 1993; Twarog et al. 1997), the range among more recent analyses is $E(B-V) = 0.10$ to 0.16. Care must be taken, however, in assigning weight to many of these values. For example, Kalirai et al. (2001) adopts without explanation $E(B-V) = 0.10$, a value later assumed without explanation by Hole et al. (2009). Anthony-Twarog et al. (2013) use the mean of the derived literature values between 0.12 and 0.16. Jeffries et al. (2013) attempt to derive the cluster reddening through a differential comparison of the clump stars in M67 and NGC 6819. However, the final value is built upon the assumption that the clump stars in NGC 6819 have uniform reddening and that NGC 6819 is more metal-rich

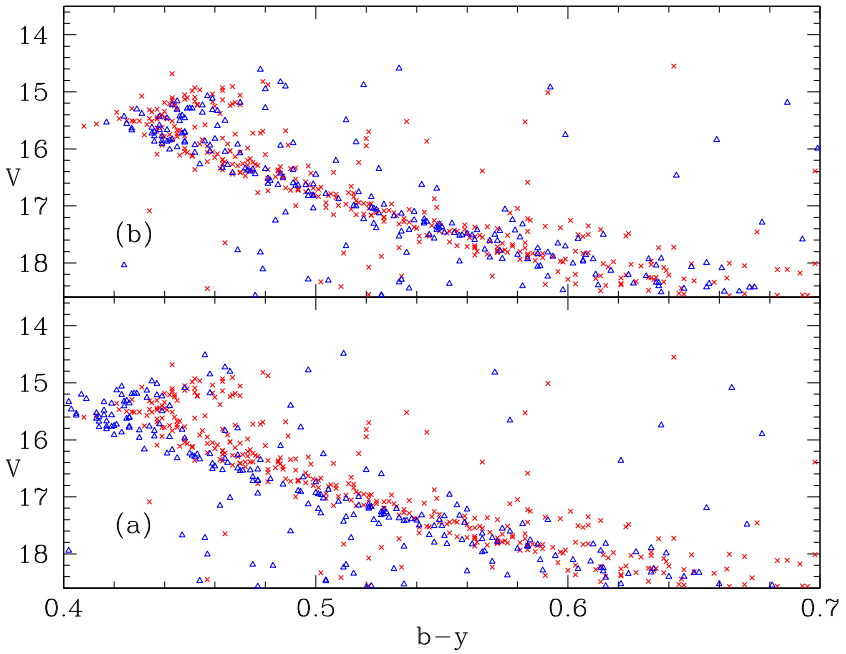

Figure 10. (a) The CMD turnoff and main sequence with stars isolated by position on the sky. Red crosses come from regions of predicted higher reddening by PL while the blue triangles come from the quadrant with the reddening minimum. (b) Same as (a), but with the blue triangles shifted in $b - y$ by +0.022 mag and V by 0.10 mag.

(A color version of this figure is available in the online journal.)

than M67 by 0.05 dex. Balona et al. (2013) investigate map-based A_V estimates from the Kepler Input Catalog (Brown et al. 2011) to obtain $E(B - V) = 0.189 \pm 0.002$ for 564 stars within 12′ of the cluster; the mean reddening rises to 0.203 $\pm$ 0.003 for cluster members. However, they default to 0.15, referring back to RV and the spectroscopic results of Bragaglia et al. (2001). Wu et al. (2014a) derive reddening through an isochrone match to the BV data of Hole et al. (2009), arriving at a simultaneous estimate of the reddening, metallicity, and distance with $E(B - V) = 0.13$ and an unrealistically small uncertainty of $\pm$0.01. In the most recent paper, Wu et al. (2014b) simply default to the mean supplied by Bragaglia et al. (2001). In summary, there are few direct, reliable estimates of the reddening to NGC 6819 which don't presume either uniform reddening and/or an assumed high metallicity. Only RV derived $E(B - V) = 0.16$ and [Fe/H] $\sim$−0.05 through isochrone matches to the BV CMD. Bragaglia et al. (2001) represents the most cited source for a reddening ($E(B - V)$ = 0.14 $\pm$ 0.04) and metallicity estimate ([Fe/H] = +0.09 $\pm$ 0.03), but these parameters are defined by 3 red clump giants, one of which is now known to be a binary (Hole et al. 2009). Friel & Janes (1993) derived [Fe/H] = +0.05 from moderate-dispersion spectroscopy, adopting $E(B - V) = 0.28$ on a scale where M67 had [Fe/H] = −0.09. The differential was revised by Twarog et al. (1997) using the same excessive reddening value, finding [Fe/H] = 0.07 on a scale where M67 has [Fe/H] = 0.00. If one adopts the correction to [Fe/H] of −0.06 dex for a decline of 0.05 in $E(B - V)$ (Friel & Janes 1993), a shift from $E(B - V) = 0.28$ to 0.16 should lower the metallicity of NGC 6819 by 0.14 dex, placing it between the metallicity of M67 and −0.07 dex lower. However, Friel et al. (2002) revise the reddening of NGC 6819 to $E(B-V) = 0.16$ and find [Fe/H] −0.11 for the cluster on a scale where M67 is fixed at −0.15. We conclude that NGC 6819 is most probably more metal poor than M67 by about −0.05 dex, rather than comparable to the Hyades in metallicity.

5. SUMMARY AND CONCLUSIONS

Recently the old open cluster, NGC 6819, has become a high profile object of considerable astrophysical interest due to its location within the Kepler field. However, apart from this particular circumstance, the cluster still would be invaluable to those focused on stellar and galactic evolution because of its rich stellar population and an age between 2 and 4 Gyr, a range shared by very few nearby objects. With the goal of deriving high-dispersion spectroscopic abundances for an extensive sample of over 300 stars, an intermediate-band photometric program was undertaken to derive the key cluster parameters of reddening and metallicity as input for estimating individual stellar parameters tied to the cluster age and distance. The need for such a study is heightened when the literature parameters for the cluster are reviewed; direct reddening estimates are few in number, low in quality, and/or often dependent upon an assumed high metallicity tied primarily to spectroscopy of three red clump stars (Bragaglia et al. 2001). Equally important, greater photometric and astrometric scrutiny of the cluster has led to a claim that the cluster suffers from variable reddening (PL), an effect never included in past derivations of the reddening or metallicity.

Using $uvbyCa\mathrm{H}\beta$ photometry of a 20′ by 20′ field of NGC 6819 collected over 3 yr, high precision photometric indices have been combined with proper-motion membership to isolate a sample of 382 single-star, unevolved F–G dwarfs on the cluster main sequence. Restricting this sample further to only 278 stars with high precision measures in all indices within the prescribed limits of the photometric calibrations leads to a mean reddening of $E(b - y) = 0.117 \pm 0.005$ or $E(B - V) = 0.160 \pm 0.007$, internal and external uncertainties included. Somewhat surprising, even with the slightly higher than usual reddening, the cluster metallicity, when derived using individual reddening values for each star or adopting a mean value for all stars, becomes [Fe/H] = −0.06, well below what

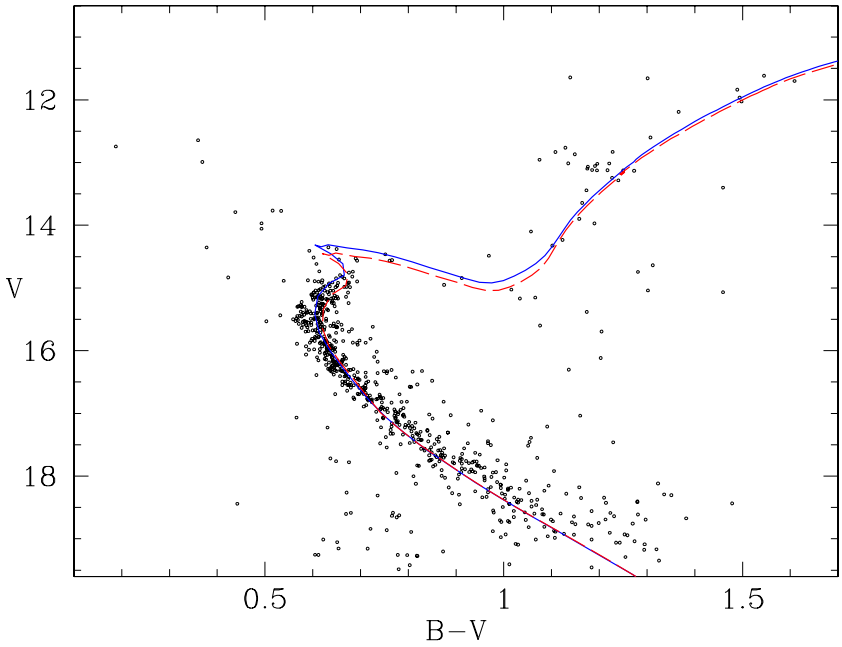

Figure 11. $(V, B-V)$ CMD of RV, corrected for the X-dependent trend of Figure 2, and individual stars corrected for variable reddening across the face of the cluster. Superposed Y^2 isochrones have [Fe/H] = −0.06 and ages of 2.3 (blue solid curve) and 2.5 Gyr (red dashed curve), adjusted with $E(B-V) = 0.16$ and $(m-M) = 12.40$. (A color version of this figure is available in the online journal.)

has become the canonical value of +0.09. Equally important, the exceptional precision of the $(V, b-y)$ photometry supplies a convincing confirmation that the cluster has higher reddening on the east side and lower reddening in the southwestern quadrant of the field. The minimum range in variation that we derive as a lower limit (0.03 mag in $E(B-V)$) is somewhat smaller than the maximum range found by PL (0.07 mag), but this may depend upon the spatial resolution of the mapping and the ability to eliminate the effect of binaries from the main sequence broadening. We conclude that the range probably lies between 0.03 and 0.06 mag in $E(B-V)$.

We close by estimating the broad impact of these changes on the derivation of the cluster distance and age, leaving a detailed star-by-star correction for a future paper dealing with the individual spectroscopic abundances (D. B. Lee-Brown et al. 2014, in preparation). Recent estimates of the cluster distance and age via a variety of techniques typically fall between $(m-M) = 12.25$ and 12.50 and 1.9 to 2.6 Gyr, respectively (Wu et al. 2014b). With the exception of RV, the studies regularly used $E(B-V)$ below 0.16 and solar metallicity or higher, with heavy emphasis on the metal-rich value from Bragaglia et al. (2001).

To test the revised reddening and metallicity, we use the BV photometry of RV, cross-identified with PL and selected to only include members with probabilities above 50%. We have applied a correction in V to the photometry of RV to adjust for the position-dependent offset illustrated in Figure 2. As a quick correction to the variable reddening, we have adjusted all the colors in the eastern zone discussed in Section 4 by −0.015 mag in $B-V$, all the colors in the delineated southwestern zone by +0.015, and left all other stars unchanged. The resulting CMD is shown in Figure 11; the main sequence and the giant branch are surprisingly tight given the simple approach to adjusting the reddening, a confirmation of the small range in reddening across the cluster face. For comparison, we have superposed a set of Y^2 (Demarque et al. 2004) isochrones with ages 2.3 (blue, solid line) and 2.5 (red, dashed line) Gyr on the data. The metallicity adopted is [Fe/H] = −0.06, with $E(B-V) = 0.16$. The zero points of the isochrones have been adjusted by −0.03 and +0.008 in M_V and $B-V$, respectively, to place them on the same system as our consistently adopted solar values. The fit to the data is very good to excellent for an age of 2.3 ± 0.2 Gyr. The distance modulus is slightly smaller than that found in Anthony-Twarog et al. (2013) due to the competing effects of raising the reddening, which should increase the apparent modulus by 0.11 mag, and lowering the metallicity by 0.15 dex, which will decrease the distance modulus by 0.18 mag (Twarog et al. 2009). Taking into account the estimated uncertainties in the absolute reddening (0.007 mag), the metallicity scale (0.05 dex), and a conservative estimate of ±0.10 mag in the ideal vertical fit of the isochrones to the data, all else being equal, one arrives at $(m-M) = 12.40 \pm 0.12$. It should be noted that this result is virtually identical to the conclusions reached by RV using a different set of isochrones; the slightly larger age (2.4 Gyr) and smaller distance modulus (12.35) are completely attributable to a bluer adopted solar color to zero their isochrones.

Extensive use was made of the WEBDA database maintained by E. Paunzen at the University of Vienna, Austria (http://www.univie.ac.at/webda). The filters used in the program were obtained by B.J.A.T. and B.A.T. through NSF grant AST-0321247 to the University of Kansas. NSF support for this project was provided to B.J.A.T. and B.A.T. through NSF grant AST-1211621 and to C.P.D. through NSF grant AST-1211699. Observing support by undergraduate Brian Schafer is gratefully acknowledged.

REFERENCES

Anthony-Twarog, B. J., Deliyannis, C. P., Rich, E., & Twarog, B. A. 2013, ApJL, 767, L19
Anthony-Twarog, B. J., Deliyannis, C. P., Twarog, B. A., Croxall, K. V., & Cummings, J. 2009, AJ, 138, 1171

Anthony-Twarog, B. J., Deliyannis, C. P., Twarog, B. A., Cummings, J. D., & Maderak, R. M. 2010, AJ, 139, 2034
Anthony-Twarog, B. J., & Twarog, B. A. 2000, AJ, 119, 2282
Anthony-Twarog, B. J., & Twarog, B. A. 2004, AJ, 127, 1000
Anthony-Twarog, B. J., Twarog, B. A., & Mayer, L. 2007, AJ, 133, 1585
Auner, G. 1974, A&AS, 13, 143
Balona, L. A., Medupe, T., Abedigamba, O. P., et al. 2013, MNRAS, 430, 3472
Bragaglia, A., Carretta, E., Gratton, R. G., et al. 2001, AJ, 121, 327
Brown, T. M., Latham, D. W., Everett, M. E., & Esquerdo, G. A. 2011, AJ, 142, 112
Brunker, S. W., Anthony-Twarog, B. J., Deliyannis, C., & Twarog, B. A. 2013, BAAS, 221, 250.28
Burkhead, M. S. 1971, AJ, 76, 251
Carraro, G., Anthony-Twarog, B. J., Costa, E., Jones, B. J., & Twarog, B. A. 2011, AJ, 142, 127
Carraro, G., Giorgi, E., Costa, E., & Vazquez, R. A. 2014, MNRAS, 441, L36
Crawford, D. L. 1975, AJ, 80, 955
Crawford, D. L. 1979, AJ, 84, 1858
Cummings, J. D., Deliyannis, C. P., Anthony-Twarog, B. J., Twarog, B. A., & Maderak, R. M. 2012, AJ, 144, 137
Demarque, P., Woo, J. -H., Kim, Y. -C., & Yi, S. K. 2004, ApJS, 155, 667 (Y^2)
Friel, E. D., & Janes, K. A. 1993, A&A, 267, 75
Friel, E. D., Janes, K. A., Tavarez, M., et al. 2002, AJ, 124, 2693
Gim, M., VandenBerg, D. A., Stetson, P. B., Hesser, J. E., & Zurek, D. R. 1998, PASP, 110, 1318
Hauck, B., & Mermilliod, M. 1998, A&AS, 129, 431
Hole, K. T., Geller, A. M., Mathieu, R. D., et al. 2009, AJ, 138, 159
Janes, K. A., & Phelps, R. L. 1994, AJ, 108, 1773
Jeffries, M. W., Sandquist, E. L., Mathieu, R. D., et al. 2013, AJ, 146, 58
Kalirai, J. S., Richer, H. B., Fahlman, G. G., et al. 2001, AJ, 122, 266 (KA)
Lamers, H. J. G. L. M., Gieles, M., Bastian, N., et al. 2005, A&A, 441, 117
Lindoff, U. 1972, A&AS, 7, 497
Nissen, P. E. 1988, A&A, 199, 146
Nissen, P. E., Twarog, B. A., & Crawford, D. L. 1987, AJ, 93, 634
Olsen, E. H. 1983, A&AS, 54, 55
Olsen, E. H. 1988, A&A, 189, 173
Olsen, E. H. 1993, A&AS, 102, 89
Olsen, E. H. 1994, A&AS, 106, 257
Platais, I., Gosnell, N. M., Meibom, S., et al. 2013, AJ, 146, 43 (PL)
Rosvick, J., & VandenBerg, D. A. 1998, AJ, 115, 1516 (RV)
Schmidt, E. G. 1976, PASP, 88, 6
Schuster, W. J., & Nissen, P. E. 1989, A&A, 221, 65
Stello, D., Meibom, S., Gilliland, R. L., et al. 2011, ApJ, 739, 13
Twarog, B. A., & Anthony-Twarog, B. J. 1995, AJ, 109, 2828
Twarog, B. A., Anthony-Twarog, B. J., & De Lee, N. 2003, AJ, 125, 1383
Twarog, B. A., Anthony-Twarog, B. J., & Edgington-Giordano, F. 2009, PASP, 121, 1312
Twarog, B. A., Ashman, K., & Anthony-Twarog, B. A. 1997, AJ, 114, 2556
Twarog, B. A., Corder, S., & Anthony-Twarog, B. J. 2006, AJ, 132, 299
Wu, T., Li, Y., & Hekker, S. 2014a, ApJ, 781, 44
Wu, T., Li, Y., & Hekker, S. 2014b, ApJ, 786, 10
Yang, S.-C., Sarajedini, A., Deliyannis, C. P., et al. 2013, ApJ, 762, 3 (YA)